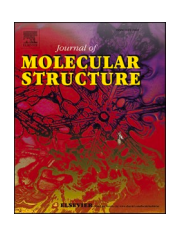
ELSEVIER

Contents lists available at ScienceDirect

# Journal of Molecular Structure

journal homepage: www.elsevier.com/locate/molstr





# Vibrational spectroscopy and structural characterization of neutral and cationic hydroxyacetone

Ende Huang <sup>a,b</sup>, Siyue Liu <sup>a,c</sup>, Xiaohu Zhou <sup>a</sup>, Licheng Zhong <sup>a</sup>, Shuze Ma <sup>a,b</sup>, Ransheng Wang <sup>a,b</sup>, Hongwei Li <sup>a</sup>, Jinrong Yang <sup>d</sup>, Xiao He <sup>d,e</sup>, Wenrui Dong <sup>a,f,\*</sup>, Xueming Yang <sup>a,g</sup>

- a State Key Laboratory of Molecular Reaction Dynamics, Dalian Institute of Chemical Physics, Chinese Academy of Sciences, Dalian, 116023, China
- b University of Chinese Academy of Sciences, Beijing, 100049, China
- <sup>c</sup> Key Laboratory of Materials Modification by Laser, Ion, and Electron Beams, Chinese Ministry of Education, School of Physics, Dalian University of Technology, Dalian, 116024 China
- d Shanghai Engineering Research Center of Molecular Therapeutics and New Drug Development, Shanghai Frontiers Science Center of Molecule Intelligent Syntheses, School of Chemistry and Molecular Engineering, East China Normal University, Shanghai, 200062, China
- e New York University-East China Normal University Center for Computational, 18 Chemistry, New York University Shanghai, Shanghai, 200062, China
- f Hefei National Laboratory, Hefei, 230088, China
- <sup>g</sup> Department of Chemistry, Southern University of Science and Technology, Shenzhen, 518055, China

#### ARTICLE INFO

#### Keywords: Molecular structure Cationic structure Infrared spectroscopy

#### ABSTRACT

In this study, we utilized the infrared (IR)–vacuum-ultraviolet (VUV) non-resonant ionization and fragmentation detected IR spectroscopy (NRIFD-IR) technique to explore the IR spectra (2700–7200 cm<sup>-1</sup>) and the structures of both neutral and cationic hydroxyacetone. By comparing the experimentally obtained IR spectra with the anharmonic frequencies calculated at the B2PLYP-D3/cc-pVTZ and B3LYP-D3(BJ)/def2-TZVPP level of theory, we assigned the structures of hydroxyacetone and its cation. Notably, we observed a discrepancy in the neutral spectrum within the CH stretch region, depending on whether the parent or fragment channel was monitored. This observation suggests that the near-threshold dissociative ionization process exhibits mode-selectivity, implying that certain vibrational modes play a crucial role in either facilitating or inhibiting the dissociation event.

# 1. Introduction

Hydroxyacetone (HA), also known as acetol (CH<sub>3</sub>C(O)CH<sub>2</sub>OH), is a colorless, distillable liquid organic compound that has attracted considerable attention from various perspectives. As the methyl derivative of glycolaldehyde, the simplest sugar component, and the most basic hydroxy ketone structure with adjacent oxygen atoms on its carbon backbone, HA represents the next level of molecular complexity among the smallest sugar molecules from an astrophysical perspective [1]. These carbohydrates are believed to serve as energy storage and participate in the formation of DNA and RNA [2]. Despite being proposed as an interstellar molecule in 2006, insufficient evidence was found to claim its detection due to the absence of several transitions at 2 and 3 mm during a search towards Sagittarius B2(N) using the Arizona Radio Observatory (ARO) 12 m telescope [1]. It was not until 2020 that HA was successfully detected in the solar-type protostar IRAS 16,

293–2422 B using the Atacama Large Millimeter Array science verification data [3]. Beyond its astrophysical significance, HA is well-recognized as a valuable starting material for the synthesis of important organic compounds, such as gem-diols, acetals, and ketals [4]. Moreover, HA, along with methacrolein (MTA) and methyl vinyl ketone (MVK), has been identified as a secondary carbonyl product of isoprene oxidation [5,6], and observed as a stable end product from reactions of the (CH<sub>3</sub>)<sub>2</sub>COO Criegee intermediate [7]. Recent studies have employed a combination of infrared and Raman spectroscopy, supported by computational methods, to achieve a comprehensive vibrational analysis of MVK, providing accurate spectral assignments [8]. In the troposphere, the reactive pathways of biogenic hydrocarbons are expected to occur via its reaction with OH or through photolysis, with the rate and mechanism determined by Orlando and Dillon [6,9].

To date, the vibrational spectra of HA have not been comprehensively characterized. Mohaček-Grošev reported the IR spectra of HA in

E-mail address: wrdong@dicp.ac.cn (W. Dong).

 $<sup>^{\</sup>ast}$  Corresponding author.

the liquid phase, concentrating on the IR range region below 3500 cm<sup>-1</sup> [2]. Sharma et al. examined the structure of HA isolated in an argon matrix at 12 K and in a pristine solid phase across the temperature range of 12-175 K [10]. They compared experimental IR spectra obtained via Fourier transform infrared (FTIR) spectroscopy with theoretical spectra derived from both ab initio (MP2) and density functional theory (DFT) calculations. Their results indicated that the observed IR spectra correspond exclusively to the most stable Cc conformer. Lindenmaier et al. methodically assigned the fundamental vibrational modes of HA using gas-phase IR, far-IR, Raman spectroscopy, and ab initio methods [11], and attributed some of the observed IR spectra to different vibrational modes than those identified by Sharma et al. Gordon et al. investigated the IR spectra of HA at the air-water interface through a combination of experimental techniques, including vibrational sum frequency spectroscopy and surface tensiometry, as well as computational approaches such as molecular dynamics simulations and DFT calculations [12]. Their study provided detailed information on the conformational distributions and hydrogen-bonding interactions of HA at the interface.

In the fundamental region of the HA infrared (IR) spectra, discrepancies persist in the assignment of vibrational modes, and several theoretically predicted modes remain unobserved. Additionally, the IR spectra in the overtone region are absent, as are the IR spectra for cationic HA.

In this study, we present an in-depth analysis of the vibrational spectra of both neutral and cationic HA spanning the range from 2700 to 7200 cm<sup>-1</sup>. By integrating observed and computed vibrational spectra with structural data of HA, we have successfully identified the spectral carriers for both neutral and cationic HA species.

#### 2. Methodology

## 2.1. Experimental section

In this study, the infrared (IR)–vacuum-ultraviolet (VUV) non-resonant ionization and fragmentation detected IR (NRIFD-IR) spectroscopy technique was employed to ascertain the IR spectra of both neutral and cationic HA molecules. The NRIFD-IR approach involved the usage of a VUV laser for single-photon ionization or dissociative ionization of the neutral compounds. For acquiring the IR spectra of the neutral species, the IR laser pulse was introduced prior to the VUV laser pulse; conversely, for the IR spectra of the cationic species, the IR laser pulse succeeded the VUV laser pulse. The IR spectra were determined by the differential signals obtained from the target species or their fragments, with and without IR irradiation. By observing the variance in signal intensities of neutral HA (m/z=74) and its dissociative ionization products (m/z=43) upon exposure to VUV radiation, both in the presence and absence of IR radiation absorption, we successfully derived the IR spectra for the neutral and cationic states of HA.

The experimental apparatus, comprising of a vacuum ultraviolet (VUV) ionization source synchronized with an infrared (IR) laser and a time-of-flight mass spectrometer (TOFMS), has been previously detailed elsewhere [13]; a brief overview is presented herein. The helium-entrained anhydrous HA (>98 %, TCI Shanghai Development Co., Ltd) was entrained in helium using a bubbler at a back pressure of 25 psi. The resultant gaseous mixture (approximately 0.5 % HA in Helium) was introduced into a pulsed solenoid valve (Parker, General Valve Series 9, 0.5 mm orifice, 10 Hz) to generate a molecular beam. Subsequently, the molecular beam was collimated by passing through a 1.5 mm diameter skimmer situated approximately 2 cm downstream from the valve nozzle. At the center of the extraction region of the reflectron TOFMS, the molecular beam was orthogonally intersected by counter-propagating VUV and IR lasers. The ion signal of the generated cations was amplified using an amplifier (Stanford research system, SR445A) before being transmitted to a digital storage oscilloscope (InfiniiVision DSO-X 3054A) for data acquisition and subsequent recording by a computer.

For the measurement of the IR spectra of neutral HA, we utilize the 125.280 nm (9.90 eV, 4.5  $\mu$ J/pulse) free electron laser (FEL) of Dalian Coherent Light Source (DCLS) to ionize the HA molecule (m/z=74), the ionization energy (IE) of which is reported to be (9.78  $\pm$  0.06 eV) [14]. By introducing the IR laser 50 ns prior to the FEL, the total energy absorbed by the HA molecule could exceed the appearance energy (AE) of [CH<sub>3</sub>CO]<sup>+</sup> (10.30 eV) [14,15], thereby inducing dissociative ionization of HA. The IR spectra of neutral HA were obtained by monitoring the signal changes of cationic HA (m/z=74) or its fragment [CH<sub>3</sub>CO]<sup>+</sup> (m/z=43) while scanning the IR laser from 2700 to 7200 cm<sup>-1</sup>. The IR spectra of the cationic HA were measured in an analogous manner, with the exception of employing a 118 nm (10.5 eV) laser as an ionization and dissociative ionization source, which was fired 50 ns before the IR laser.

The 118 nm VUV laser is generated by frequency-tripling of the 355 nm laser (40 mJ pulse  $^{-1}$ ), triple frequency of the output of an Nd: YAG laser (Beamtech, SGR-20, 10 Hz), in a cell containing a gaseous mixture of Xe and Ar (Xe: Ar = 1:10) at  $\sim\!280$  torr total pressure. The 118 nm laser is then focused into the center of the ionization region with a convex MgF $_2$  lens that is mounted at the end of the gas cell.

The tunable IR laser was generated by using a potassium titanyl phosphate (KTP)/potassium titanyl arsenate (KTA) optical parametric oscillator/amplifier system (OPO/OPA, Laser Vision, 0.9 cm $^{-1}$  resolution in broadband mode) pumped by a Nd: YAG laser (Continuum Surelite EX, 5 Hz, 630 mJ pulse $^{-1}$ ). The IR laser with a typical energy of 10 mJ pulse $^{-1}$  (at the entrance of the CaF $_2$  window) is focused by a CaF $_2$  lens (f=500 mm) into the ionization region.

#### 2.2. Computational section

The minimum energy conformation of the HA molecule was determined through a multi-step computational approach. Initial automated conformational searches were performed utilizing the Molclus gentor module [16], involving the rotation of single bonds (C5-C7 and C7-O10). Subsequently, all initial geometries of neutral HA were optimized using density functional theory (DFT) calculations. These calculations employed the B3LYP functional with the def2-TZVPP basis set and Grimme's D3(BJ) dispersion correction, including Becke-Johnson damping and three-body terms [17-19].

Four equilibrium structures for neutral HA (Cc, Tt, Tg, Ct, listed in order of increasing energy) were identified. These conformers are further discussed in Section 3.1.1. Cationic conformers were derived from these four equilibrium structures of neutral HA by altering the charge and spin multiplicity to 1 and 2, respectively. Further optimization at the B3LYP-D3(BJ)/def2-TZVPP level yielded the structures of cationic HA-Tg' and HA-Cg.

Calculations employed the appropriate DFT formalism: restricted DFT (RDFT) for closed-shell species (HA and  $\mathrm{CH_{3}CO^{+}}$ ) and unrestricted DFT (UDFT) for open-shell species (HA<sup>+</sup> and  $\mathrm{CH_{2}OH}$ ). This principle was also followed for the anharmonic frequency calculations at the B2PLYP-D3/cc-pVTZ level. All computations were performed using the Gaussian 16 program suite [20].

Based on the optimized geometries, The relative single-point energies of these conformers, expressed in kcal/mol, have been calculated using the RIJK-CCSD(F12\*)(T\*)/cc-pVTZ-F12//B3LYP-D3(BJ)/def2-TZVPP level of theory, as implemented in the ORCA quantum chemistry software package [21]. These energy values have been subjected to zero-point energy corrections for improved accuracy.

The anharmonic IR absorption spectra of the neutral and cationic HA species were computed using the second-order vibrational perturbation theory (VPT2) method, as implemented in the Gaussian 16 software. Given our IR spectra scanning range of 2700–7200 cm<sup>-1</sup>, which encompasses overtones and combination modes, anharmonic frequency calculations were essential. For cationic HA, we selected the B3LYP-D3 (BJ)/def2-TZVPP method due to its optimal balance of accuracy and computational efficiency. This approach provides high-grade triple-zeta basis accuracy and incorporates dispersion functions suitable for our

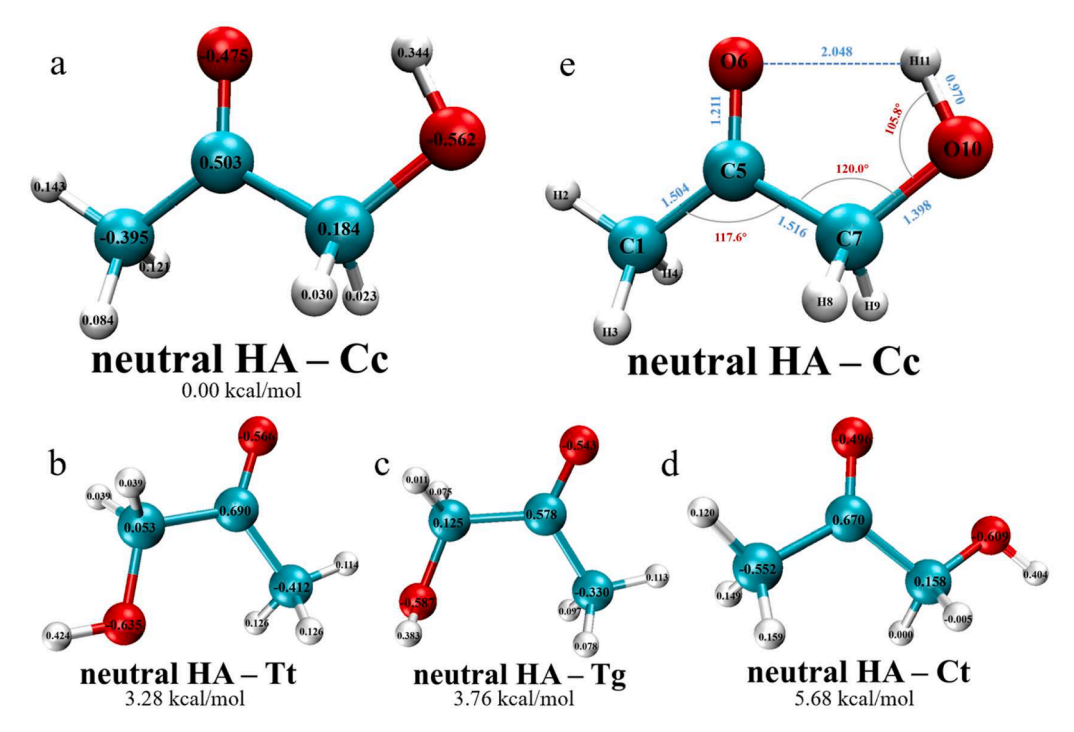


Fig. 1. Geometrically optimized and energetically stable conformations of four neutral HA conformers (Fig. 1a to 1d) and the electrostatic potential charges (Fig. 1a to 1d). The figure also highlights the pivotal bond lengths and bond angles that play a crucial role in determining the structural characteristics of neutral HA-Cc (Fig. 1e).

cationic HA system. The results obtained align well with our experimental data for cationic HA.

For neutral HA, the presence of intramolecular hydrogen bonding increased system complexity. Additionally, we observed a significant discrepancy between the calculated  $\nu_{\rm OH}$  (3492.3 cm $^{-1}$ ) and our experimental results (3522.4 cm $^{-1}$ ) using B3LYP-D3(BJ)/def2-TZVPP. Consequently, we opted for the B2PLYP-D3/cc-pVTZ method, renowned for its accuracy in describing radical systems and zwitterions [22,23]. This double-hybrid functional with cc-pVTZ basis provides superior accuracy compared to B3LYP-D3(BJ)/def2-TZVPP for neutral HA, as demonstrated in Table S5.

We also applied B2PLYP-D3/cc-pVTZ to calculate anharmonic frequencies for cationic HA (Table S7). Both methods yielded appropriate results for attributing our cationic HA spectra. However, due to methodological differences, calculations using B3LYP-D3(BJ)/def2-TZVPP showed better agreement with our experimental spectra compared to the double-hybrid results for the  $\nu_6$  mode and modes from the  $2\nu_{\text{CH}}$  region. Therefore, we chose to use B3LYP-D3(BJ)/def2-TZVPP results for attributing our cationic spectra.

Natural Bond Orbital (NBO) analyses of the neutral and cationic HA molecules were conducted using the integrated NBO 3.1 program within the Gaussian16 software package at the B3LYP/def2-TZVPP level of theory. We employed the Multifunctional Wavefunction Analyzer (Multiwfn) program [24] to perform orbital interaction, Merz-Kollmann (MK) electrostatic potential (ESP) fitting for atomic charges, and Mayer bond order calculations. These analyses were based on wavefunction files generated by the Gaussian16 software package. Visualization of the results was achieved using a combination of the Multiwfn and Visual Molecular Dynamics (VMD) software packages [25].

#### 3. Results and discussion

#### 3.1. Structure of neutral and cationic HA

# 3.1.1. Neutral HA

HA exists in four distinct equilibrium structures, differing in the

orientation of the O = C—C-O and H—O-C—C dihedral angles, as confirmed by previous theoretical investigations [10,26]. In this study, we adopted the nomenclature proposed by Sharma et al. [10], where the capital letters (T, C, G, G') denote the orientation around the O = C—C-O dihedral angle, and the lowercase letters (t, c, g, g') refer to the H—O-C—C dihedral angle. The corresponding dihedral angle ranges are as follows:  $-45^\circ \leq (C,c) \leq 45^\circ \leq (G,g) \leq 135^\circ \leq (T,t) \leq 225^\circ \leq (G',g') \leq 315^\circ$ . Among the four conformers, the Cc conformer exhibits the lowest energy, which can be attributed to the presence of a stabilizing intramolecular hydrogen bond between the hydroxyl hydrogen and the carbonyl oxygen. Conversely, the Ct conformer possesses the highest energy  $(\Delta_{ZPE}=5.68~kcal~mol^{-1})$  due to the repulsive interactions between the two oxygen atoms in this configuration. The four neutral conformers and their relative single-point energies are depicted in Fig.1a-1d.

The second lowest energy conformer, Tt, lies 3.28 kcal mol<sup>-1</sup> above the Cc conformer. To assess the population distribution of these conformers, Boltzmann distribution calculations were performed for temperatures ranging from 0 to 350 K based on the Gibbs free energies, as presented in Table S1. The results clearly indicate that the Cc conformer is expected to be the dominant species at temperatures below room temperature, with a Boltzmann weight exceeding 99 %.

The intramolecular hydrogen bond in the molecule results in a coplanar arrangement of atoms O6, C5, C7, O10, and H11. Despite a slight torsion of the methyl group in neutral HA-Cc, as indicated by the H2-C1-C5-O6 dihedral angle of 19.6°, we consider C1 and H2 to be effectively coplanar with this arrangement. This O6-C5-C7-O10 plane serves as the reference for describing vibrational modes of both methyl and hydroxyl groups in neutral and cationic HA. For instance, terms such as "OH in-plane wag" or "methyl out-of-plane symmetric CH stretch" are defined relative to this plane, consistent with previous literature [11].

# 3.1.2. Cationic HA

In contrast to the neutral HA, we have observed that the cationic form of HA exhibits a reduced propensity to engage in intramolecular

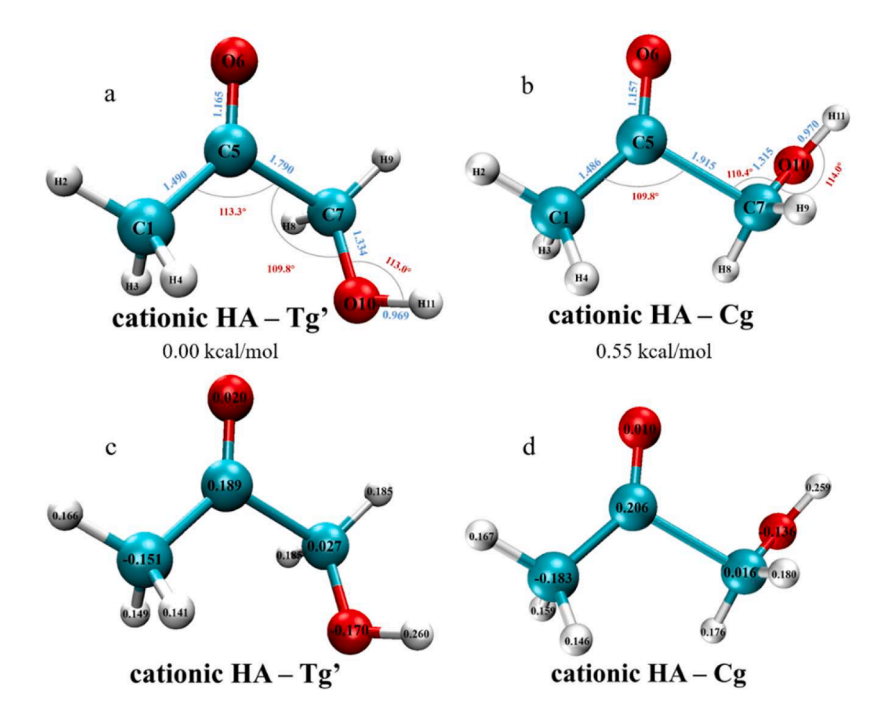


Fig. 2. Geometrically optimized and energetically stable conformations of two cationic HA conformers (Fig. 2a and 2b) and the electrostatic potential charges (Fig. 2c and 2d). The figure also highlights the pivotal bond lengths and bond angles that play a crucial role in determining the structural characteristics of cationic HA-Tg' and HA-Cg.

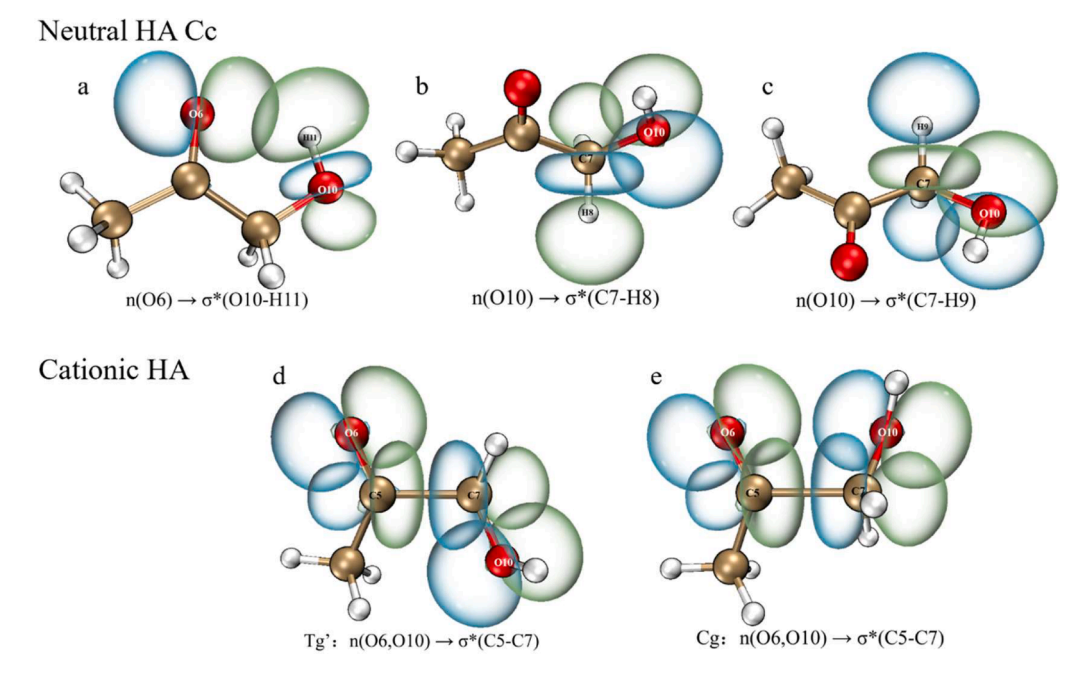


Fig. 3. Natural bond orbital (NBO) analysis of orbital interactions in neutral and cationic conformers of HA-Cc. In neutral HA-Cc (a-c), the NBO plots demonstrate the overlap between antibonding orbitals ( $\sigma^*$ ) of O–H or C–H and lone pair (n) orbitals of O6 and O10. In the cationic conformers (d and e), the overlap occurs between lone pair (n) orbitals of oxygen and the antibonding orbital ( $\sigma^*$ ) of the C5–C7 bond. NBO calculations were performed using the B3LYP functional in conjunction with the def2-TZVPP basis set, employing the pop=nboread keyword. The isodensity surface is visualized at a value of 0.05, providing a clear representation of the orbital interactions.

hydrogen bonding. The equilibrium conformations of the H-O-C-C dihedral angle demonstrate a preference for the gauche orientation, resulting in the identification of only two conformers, namely Tg' and Cg (depicted in Fig. 2a and 2b). Consequently, due to the repulsive forces between the oxygen atoms, the second most energetically favorable conformer, cationic HA-Cg, possesses a single-point energy that is approximately 0.55 kcal mol<sup>-1</sup> higher in comparison to that of the

cationic HA-Tg' conformer.

The Gaussian 16 package considers only the total charge for the system, precluding the localization of charge on specific atoms in cationic HA. To address this limitation and mitigate the influence of dispersion functions on Mulliken charge results, we employed the Multiwfn program to evaluate MK ESP fitting charges based on wavefunctions obtained from Gaussian 16. Our analysis revealed that the

Table 1 Ionization energies (IE) and fragment appearance energies (AE) of HA.

Ion	Product	IE/AE (eV)	
m/z = 74	[CH3C(O)CH2OH] <sup>+</sup>	10.00 [15] 9.78 [14,27]	
m/z = 73	$[C_3H_5O_2]^+ + H$	11.60 [14,27]	
m/z = 57	$[C_3H_5O]^+ + OH$	11.26 [14,28]	
m/z = 45	$[C_2H_5O]^+ + HCO$	10.21 [14,29]	
m/z = 43	$[CH_3CO]^+ + CH_2OH$	10.30 [14,15,30]	
m/z=31	${\rm [CH_2OH]}^+ + {\rm CH_3CO}$	11.29 [14]	

charge in both cationic Tg' and Cg species is predominantly centered on the C5 and H11 atoms.

## 3.1.3. NBO analysis

NBO analysis was performed on the neutral HA-Cc, cationic HA-Tg', and HA-Cg using the B3LYP method with the def2-TZVPP basis set, and the results are presented in Table S2. Fig. 3 illustrates the NBO plot of the interaction between the lone pair n(O) orbital, showcasing the difference between neutral and cationic HA. The optimized structures of cationic HA-Tg' and HA-Cg differ from that of neutral HA-Cc (depicted in Figs. 1e, and Fig. 2a, 2b) in several aspects.

Firstly, the dihedral angle of H—O-C—C changes from  $3.1^\circ$  (Cc) to  $-100.0^\circ$  (Tg') or  $-86.2^\circ$ (Cg) due to the change in the electrical charge of the carbonyl oxygen (O6) from negative to positive, resulting in a repulsive force with the positively charged hydroxyl hydrogen.

Secondly, the bond length of C7-O10 is reduced from 1.40 Å to 1.33 Å, as a consequence of the gauche structure of cationic HA. In this structure, the lone pair n(O10) orbital exhibits minimal interaction with the two neighboring methylene  $\sigma^*$  bond orbitals (C7-H8 and C7-H9). In contrast, the second-order perturbation energy for n(O10)  $\rightarrow \sigma^*$ (C7-H8) and n(O10)  $\rightarrow \sigma^*$ (C7-H9) in neutral HA are 8.51 and 7.34 kcal mol<sup>-1</sup>, respectively (shown in Fig. 3b and 3c). This difference accounted for a

redshift of approximately 150 cm<sup>-1</sup> in the methylene asymmetric CH stretch bands of cationic HA compared to neutral HA. (See Table S3-S9 in the Supporting Information)

Finally, accompanied by an elongation of the C5-C7 bond from 1.52 Å to more than 1.79 Å, the Mayer bond order of C5-C7 decreases from 0.96 to 0.56 (at the B3LYP/def2-TZVPP level). This suggests that the excited cationic HA can readily transform to  $CH_3CO^+$  and  $CH_2OH$  through the cleavage of the C5-C7 bond, which is the primary dissociation channel, as shown in Table 1.

The NBO analysis can be employed to justify the dissociation preference of cationic HA in the C5-C7 bond, which is attributed to the spatial proximity of the C5-C7 bond and the two oxygen atoms with lone pair orbitals. Notably, the gauche tendency in cationic HA can be effectively described by the preference for better overlap of the lone pair n(10) orbital with the C5-C7 *anti*-bond. The orbital interaction analysis for cationic HA-Tg' has been employed to elucidate this issue, and we will discuss it further in Section 3.5.

## 3. 2. VUV photoionization mass spectra of HA

Table 1 presents a series of dissociative ionization products of HA, resulting from various dissociation pathways. These pathways include simple bond cleavage, which forms  $C_3H_5O_2^+$  (m/z=73),  $CH_3CO^+$  (m/z=43), and  $CH_2OH^+$  (m/z=31), as well as more complex processes involving hydrogen migrations from the methyl group to the carbonyl oxygen, followed by OH dissociation to form  $C_3H_5O^+$  (m/z=57). Additionally, rearrangement to  $CH_3CH(OH)CHO$  and subsequent bond cleavage can yield  $C_2H_5O^+$  (m/z=45), as suggested by a previous study using synchrotron radiation as the ionization source [14].

Fig. 4 displays the mass spectra of HA obtained using a time-of-flight mass spectrometer. As shown in Fig. 4a and 4b, the resonant absorption of infrared photons with a frequency of 2908  $\rm cm^{-1}$  (0.36 eV) prior to the ionization by 125.2 nm (9.90 eV) FEL radiation enhances the ionization

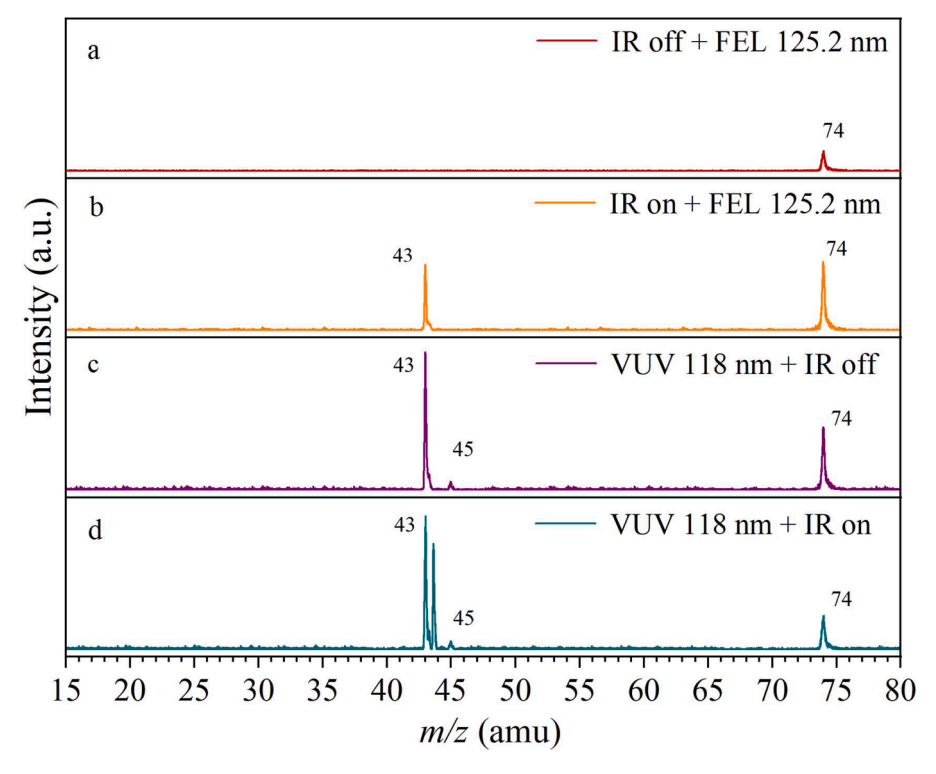


Fig. 4. Mass spectra of HA and its fragmentation products obtained using two distinct photoionization techniques. Fig. 4a and 4b show the results of using a free-electron laser (FEL) operating at 125.2 nm, where the introduction of IR radiation prior to FEL induces the fragmentation of the parent ion  $CH_3CO(CH_2OH^+)$  (m/z = 74) into the fragment ion  $CH_3CO^+(m/z = 43)$ . Fig. 4c and 4d display the results of using vacuum ultraviolet (VUV) radiation at 118 nm, where the subsequent introduction of IR radiation induces further fragmentation of HA cations, generating  $CH_3CO^+(m/z = 43)$ , which appeared as a separate peak between m/z = 43 and 45. Notably, the spectra in panels (b) and (d) were acquired with the assistance of an IR laser operating at a wavenumber of 2908 cm<sup>-1</sup>.

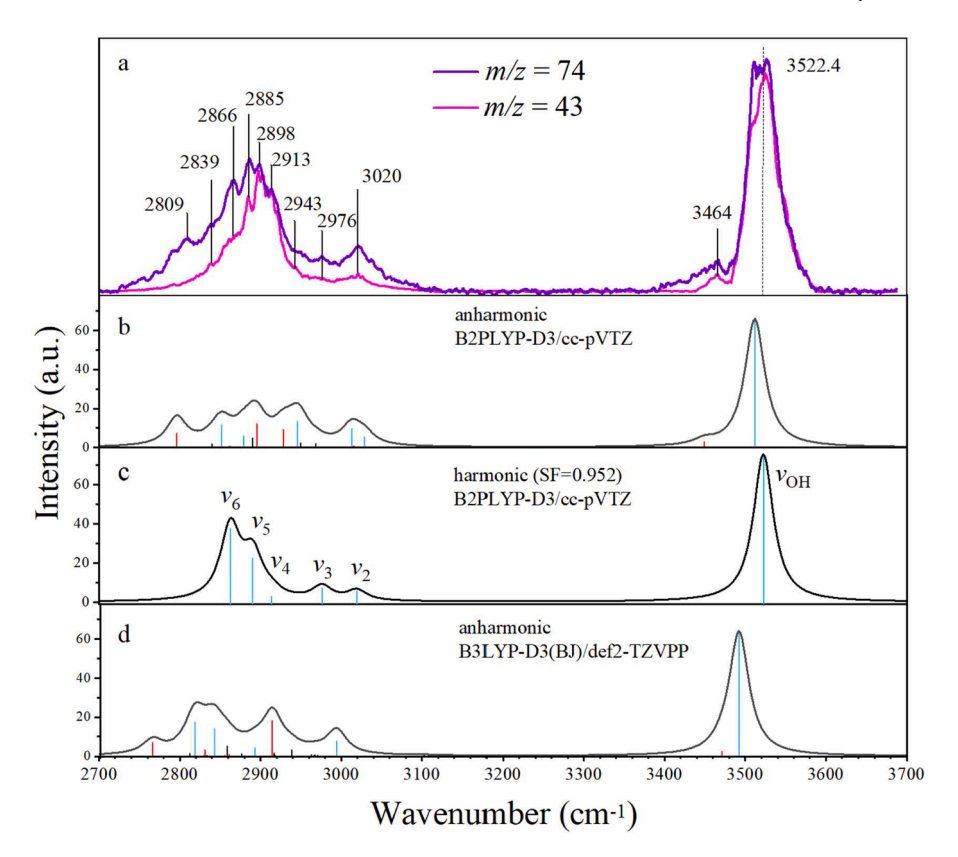


Fig. 5. IR spectra of neutral HA in the fundamental vibrational region. (a) Experimental IR spectrum was obtained from both parent and fragment channels. Intensities were normalized to the OH stretching mode, with peak positions explicitly labeled, facilitating direct comparison. (b) and (c) Computed anharmonic and harmonic IR spectra, respectively, at the B2PLYP-D3/cc-pVTZ level of theory. The harmonic IR spectrum was scaled by a factor of 0.952 to account for anharmonicity effects. (d) Calculated anharmonic IR spectrum at the B3LYP-D3(BJ)/def2-TZVPP level of theory. To simulate spectral broadening in (a), the stick spectra in (b-d) were convoluted with a Lorentzian profile (full width at half maximum (FWHM) of 30 cm<sup>-1</sup>). In the calculated spectra, fundamental, overtone, and combination modes are represented by blue, red, and black lines, respectively.

probability of HA and facilitates the formation of the dissociative ionization product  $\text{CH}_3\text{CO}^+$  (m/z=43). The total energy of the IR and VUV photons (10.35 eV) exceeds the appearance energy of the  $\text{CH}_3\text{CO}^+$  fragment, resulting in its appearance in Fig. 4b. The continuous increase in the photoionization efficiency curve of HA from 9.78 to 10.35 eV explains the increment in the m/z=74 signal in Fig. 4b.

Fig. 4c and 4d illustrate the appearance of CH<sub>3</sub>CO cations in the absence of the IR laser and when the IR laser (2908 cm<sup>-1</sup>) is fired 100 ns after the 118 nm VUV laser pulse, respectively. When the IR laser is fired subsequent to the 118 nm VUV laser, resonant absorption of IR photons can dissociate the HA cation, which is initially generated by the VUV laser, as long as the total photon energy exceeds the dissociation energy of the corresponding channel. Consequently, the formation of CH<sub>3</sub>CO cations, as illustrated in Fig. 4d, occurs through two distinct pathways: (1) dissociative ionization of HA molecules by the VUV laser, resulting in a peak at m/z = 43 (Fig. 4c and 4d), and (2) IR laser-induced dissociation of the HA cations, which are initially produced by the 118 nm VUV laser. This process is characterized by the peak between m/z = 43 and 44 in Fig. 4d. The observed dislocation of the CH<sub>3</sub>CO cations in the mass spectra from the second pathway, relative to the first, can be attributed to their delayed formation. This delay occurs because these cations initially existed as HA cations before the arrival of IR radiation. Furthermore, the greater mass of HA cations results in a slower flight velocity compared to CH3CO cations, contributing to their delayed arrival (CH<sub>3</sub>CO cations produced via the second pathway, compared to those from the first pathway) at the MCP detector. Notably, the IR spectra of the HA cation are obtained by subtracting the HA or CH<sub>3</sub>CO cation signal without IR radiation from that with IR radiation. To enhance the signal-to-noise ratio of the observed IR spectra, it is

desirable to separate the two  $\rm CH_3CO$  cation sources completely. Therefore, the IR radiation is set to fire with a longer delay relative to the 118 nm laser, specifically 100 ns in this case.

# 3.3. IR spectra of neutral HA

The IR spectra of neutral HA molecules were acquired by simultaneously monitoring the parent ion (m/z=74) and its fragment ion (m/z=43) while scanning the IR laser across the spectral range of 2700–3700 cm<sup>-1</sup> (Fig. 5a). Both spectra in Fig. 5a represent the IR spectra of HA, as the IR laser was introduced before the 125.2 nm laser.

The calculated anharmonic and harmonic frequencies of the HA-Cc conformer, obtained using B2PLYP-D3/cc-pVTZ method, are presented in Fig. 5b and 5c, respectively. Initially, we employed a frequency scaling factor of 0.961 for B2PLYP-D3/cc-pVTZ, as reported in the literature [31]. However, the poor agreement between the scaled  $v_{OH}$ (3698.6 to 3554.3 cm<sup>-1</sup>) and our experimental  $v_{OH}$  frequency (3522.4 cm<sup>-1</sup>) prompted us to derive a custom scaling factor. Following previous approaches [32], we used three well-resolved peaks ( $v_{OH}$ ,  $v_2$ , and  $v_3$ ) observed in our experiments to perform a linear fit. Although limited to three data points, the fit yielded a scaling factor of 0.952 with a perfect coefficient of determination (R<sup>2</sup>=1) and a zero intercept, supporting the validity of the fitting procedure. This custom scaling factor was subsequently applied to the harmonic frequencies to account for anharmonicity effects. Additionally, the anharmonic frequencies of the HA-Cc conformer, computed using B3LYP-D3(BJ)/def2-TZVPP method, are shown in Fig. 5d. The computed IR absorption profiles of the HA-Cc conformer in Fig. 5b-d were obtained by convoluting the calculated stick spectra with a Lorentzian profile (full width at half-maximum of 30

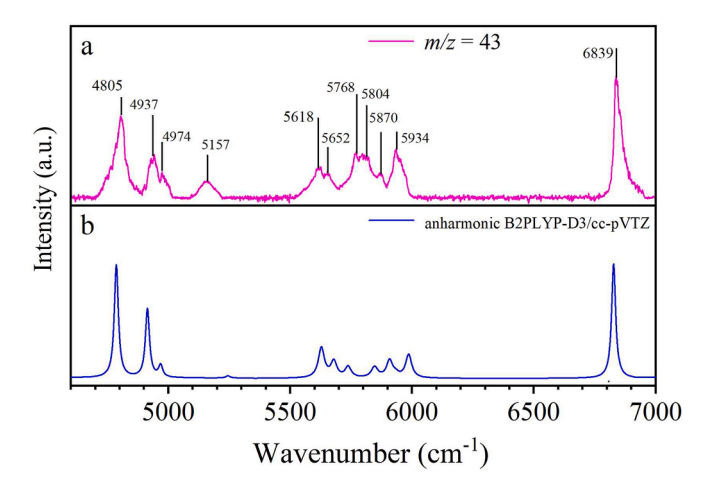


**Fig. 6.** Infrared spectra of HA in the overtone and combination bands region (4600–7000 cm $^{-1}$ ). (a) Experimental IR spectrum obtained by monitoring the fragment ion channel (m/z=43), with observed peak positions labeled. (b) Simulated IR spectrum generated by convoluting the stick spectrum, calculated from anharmonic frequencies of neutral HA-Cc at the B2PLYP-D3/cc-pVTZ level, with Lorentzian profiles (FWHM = 30 cm $^{-1}$ ). The corresponding stick spectra with assigned vibrational modes are provided in Supplementary Figures S4 and S5.

**Table 2**Assignment of experimentally observed features of neutral HA to calculated frequencies (anharmonic) of HA-Cc in the 4500–7000 cm<sup>-1</sup> region, computed at the B2PLYP-D3/cc-pVTZ level.

Observed features	Calculated anharmonic frequencies at B2PLYP-D3/cc-pVTZ			
position (cm <sup>-1</sup> )	mode	position (cm <sup>-1</sup> ) intensities (km mol <sup>-1</sup> )		
4805	$\nu_1 + \nu_{13}$	4786.1	2.10	
4937	$\nu_1+\nu_{11}$	4913.8 1.28		
4974	$\nu_1 + \nu_8$	4967.8	0.223	
5157	$v_1 + v_7$	5244.3	0.0429	
5618	$2v_6$	5627.8	0.576	
5652	$v_5 + v_6$	5678.6	0.312	
5768	$2v_5$	5737.7	0.214	
5804	$v_3 + v_4$	5844.4	0.137	
	$2v_4$	5849.8	0.0647	
5870	$2v_3$	5907.8	0.330	
5934	$v_2 + v_3$	5984.5	0.136	
	$2v_2$	5986.4	0.310	
6839	$2v_1$	6827.4	2.14	

 $\,\mathrm{cm}^{-1}$ ). Only the IR spectra of the HA-Cc conformer are shown, as its Boltzmann distribution exceeds 99 % at or below room temperature. The stick spectra of all four neutral conformers are provided in Figure S1, and the frequencies of all 27 fundamental vibrational modes of the HA-Cc conformer are listed in Table S3.

In Fig. 5a, the prominent peak at 3522.4 cm<sup>-1</sup> is assigned to the OH stretching mode ( $v_1$ ), which exhibits a redshift compared to the typical frequency of unbound OH stretching near 3700 cm<sup>-1</sup> [33,34]. Our calculated OH stretching frequency for the Cc conformer is 3512 cm<sup>-1</sup> (Fig. 5c), suggesting that the interaction between the  $\sigma^*(O-H)$  and the nonbonding n(O) orbital of the carbonyl oxygen atom, as depicted in Fig. 3a, is slightly overestimated. This interaction, including hyperconjugative electron transfer from n(O) to  $\sigma^*(O-H)$  elongates the O—H bond, resulting in a redshift in frequency. Consistently, our calculations reveal that the three conformers (Tt, Tg, and Ct) exhibit shorter O–H bonds (approximately 0.96 Å) compared to the Cc conformer (0.97 Å), and their anharmonic frequencies exceeding 3674 cm<sup>-1</sup>, as shown in Figure S1. The absence of the OH stretch feature in the observed spectra around 3674 cm<sup>-1</sup> further supports our suggestion that the Cc conformer is the dominant spectral carrier. Additionally, we observe a feature

centered at 3464 cm<sup>-1</sup>, which is consistent with the overtone of the carbonyl CO stretch  $(2\nu_7)$  in terms of both peak position (calculated to be 3449 cm<sup>-1</sup>) and intensity (2.71 km mol<sup>-1</sup>), as shown in Tables S3 and S5. Our experimental frequencies exhibit excellent agreement with the gas-phase frequencies reported by Lindenmaier et al. [11]. Specifically, our  $\nu_1$  frequency at 3522.4 cm<sup>-1</sup> is in close proximity to their value of 3523.68 cm<sup>-1</sup>. Furthermore, our observed peak at 3464 cm<sup>-1</sup> is comparable to their observation at 3461.37 cm<sup>-1</sup>, although they did not provide a definitive assignment for this peak.

In the spectral region of  $2700-3200~\rm cm^{-1}$ , significant differences are observed between the spectral contours obtained from the parent and fragment channels, as shown in Fig. 5a. For comparison, the simulated spectral profiles from convoluting calculated stick spectra with Lorentzian profiles (FWHM  $30~\rm cm^{-1}$ ) are presented in Fig. 5b-d. Notably, the observed spectral shape of m/z=74 exhibits better alignment with the anharmonic B2PLYP-D3/cc-pVTZ contour, whereas the fragment channel spectra are more consistent with the harmonic B2PLYP-D3/cc-pVTZ contour (calculated with a scaling factor of 0.952). In the following discussion, the observed peaks are compared to the calculated anharmonic IR spectra at the B2PLYP-D3/cc-pVTZ level.

To facilitate peak assignment, we focus on the less ambiguous spectral features at the extremes of the 2700–3200 cm<sup>-1</sup> region, specifically at 3020, 2976, 2943, 2839, and 2809 cm<sup>-1</sup>. Based on the calculated absorption positions and intensities, we attribute the peak at 3020 cm<sup>-1</sup> to the in-plane methyl CH stretching mode ( $\nu_2$ ), the peak at 2976 cm<sup>-1</sup> to the out-of-plane methyl asymmetric CH stretching mode ( $\nu_3$ ), and the peak at 2943 cm<sup>-1</sup> to the out-of-plane methyl symmetric CH stretching mode ( $\nu_4$ ). These assignments are supported by the calculated values of 3028.6 cm<sup>-1</sup> and 5.47 km mol<sup>-1</sup> for  $\nu_2$ , 3013.0 cm<sup>-1</sup> and 9.65 km mol<sup>-1</sup> for  $\nu_3$ , and 2946.3 cm<sup>-1</sup> and 13.6 km mol<sup>-1</sup> for  $\nu_4$ , respectively. Our observations and assignments of  $\nu_2$  and  $\nu_3$  are in good agreement with those reported by Lindenmaier et al., who observed the corresponding peaks at 3020 and 2973 cm<sup>-1</sup>, respectively.

The relative intensities of the methyl CH stretch ( $\nu_2$ ,  $\nu_3$ , and  $\nu_4$ ) are weaker in the fragment channel compared to the HA channel, indicating incomplete intramolecular vibrational redistribution (IVR) of the methyl CH stretch excitation. This leads to less efficient dissociation of the C5-C7 bond, likely due to the methyl group being farther from the C5-C7 bond compared to the methylene group.

The peak at  $2839 \, \mathrm{cm}^{-1}$  can be attributed to the combination modes of methyl symmetric scissor and in-plane OH wag ( $\nu_{10} + \nu_{11}$ , calculated at  $2839.8 \, \mathrm{cm}^{-1}$ ,  $1.65 \, \mathrm{km} \, \mathrm{mol}^{-1}$ ). The peak at  $2809 \, \mathrm{cm}^{-1}$  is assigned to the overtone of the OH in-plane wag ( $2\nu_{11}$ , calculated at  $2796.2 \, \mathrm{cm}^{-1}$ ,  $7.27 \, \mathrm{km} \, \mathrm{mol}^{-1}$ ), consistent with the assignment of the observed peak at  $2803 \, \mathrm{cm}^{-1}$  by Lindenmaier et al. [11].. Sharma et al. reported a peak at  $2824 \, \mathrm{cm}^{-1}$  for IR absorption of HA in an Ar matrix at  $12 \, \mathrm{K}$ , but did not provide an assignment. Notably, the absence of the absorption peak at  $2809 \, \mathrm{cm}^{-1}$  in the fragment spectra suggests that this near-threshold photodissociation process is vibrationally mode-selective. It is important to note that the terminal OH group is not only spatially separated from the C5-C7 bond but also exhibits a dipole orientation perpendicular to the bond axis. Consequently, the energy associated with the in-plane OH wag excitation does not directly contribute to the dissociation of the C5-C7 bond.

After completing the above assignment, two remaining CH stretches and several combination and overtone modes with intensities stronger than 1 km mol<sup>-1</sup>, as predicted by calculations, remain to be assigned. Notably, the vibrational excitations relevant to C5 and C7 facilitate the dissociation of the C5-C7 bond, leading to similar absorption intensities in the IR spectra of both HA and its fragment m/z=43. Based on the calculated absorption positions and intensities, we assign the peaks at 2913 and 2898 cm<sup>-1</sup> to the methylene asymmetric CH stretch ( $\nu_5$ ) and methylene asymmetric CH stretch ( $\nu_6$ ), respectively, which are calculated to be at 2878.8 cm<sup>-1</sup> (5.93 km mol<sup>-1</sup>) and 2851.5 cm<sup>-1</sup> (11.6 km mol<sup>-1</sup>), respectively. Our assignments are in good agreement with those of Sharma et al. [10].. who assigned their observed peaks at 2914 and

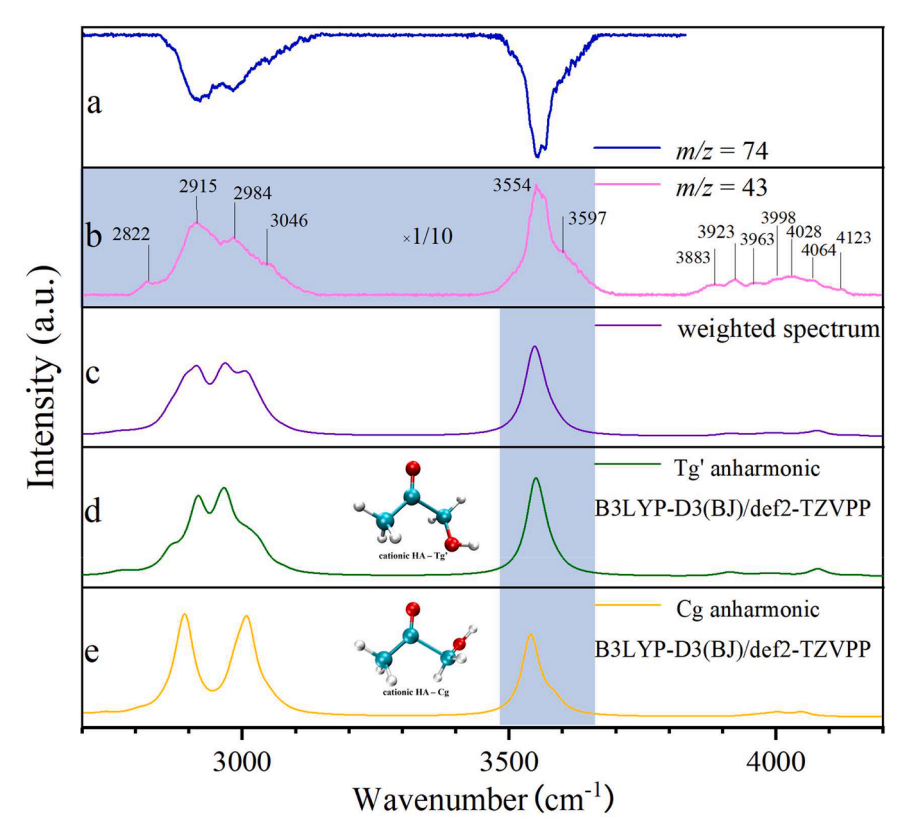


**Fig. 7.** Observed IR spectrum of cationic HA in the 2700–4200 cm<sup>-1</sup> region obtained by monitoring the HA cation (m/z = 74) (Fig. 7a) and its fragment cation (m/z = 43) (Fig. 7b). (c) Simulated anharmonic IR spectrum of cationic HA, weighted by populations of 30 % Cg conformer and 70 % Tg' conformer. (d) and (e) the simulated anharmonic IR spectra of the two cationic conformers, Tg' and Cg, respectively, calculated using the VPT2 method at the B3LYP-D3(BJ)/def2-TZVPP level of theory. The stick spectra (Table S6 in the Supporting Information) were convoluted with Lorentzian profiles (FWHM = 40 cm<sup>-1</sup>) to generate the final spectra.

**Table 3**Assignment of experimentally observed features of cationic HA to calculated anharmonic frequencies in the 2800–3700 cm<sup>-1</sup> region, computed at the B3LYP-D3(BJ)/def2-TZVPP level of theory.

Observed features	Calculated anharmonic frequencies at B3LYP-D3(BJ)/def2-TZVPP				
position (cm <sup>-1</sup> )	conformer	mode	position (cm <sup>-</sup> 1)	intensities (km mol <sup>-</sup> 1)	
2822	Tg'	$\nu_6$	2865.9	5.08	
2915	Tg'	$v_4$	2916.7	18.3	
	Cg	$v_4$	2893.3	24.9	
2984	Tg'	$2v_8$	2969.7	10.2	
	Cg	$v_3$	3010.0	19.9	
3046	Tg'	$v_5$	3032.2	3.04	
	Cg	$v_5$	3047.4	2.32	
3554	Tg'	$\nu_1$	3548.6	251	
	Cg	$\nu_1$	3540.0	229	
3597	Tg'	$v_5 + v_{20}$	3564.0	5.11	
	Cg	$\nu_1{+}\nu_{26}$	3584.4	3.39	

2897 cm<sup>-1</sup> to  $v_5$  and  $v_6$ , respectively.

The discrepancies between our experimental observations and calculations for  $\nu_5$  and  $\nu_6$  are 34 and 46 cm $^{-1}$ , respectively. The anharmonic frequencies for  $\nu_5$  and  $\nu_6$  modes were calculated considering the anharmonicity from the Coriolis X Matrix and resonance with other states. Our analysis reveals that resonance interactions play a crucial role in determining the vibrational energies of these modes. Specifically,  $\nu_5$  experiences resonance interactions with  $\nu_3$  and  $\nu_6$ , while  $\nu_6$  interacts with  $2\nu_8$  and  $\nu_8+\nu_9$ . These interactions generally result in a reduction of vibrational energy for both modes, except that the resonance between  $\nu_5$  and  $\nu_6$  causes a decrease in  $\nu_6$  while simultaneously increasing  $\nu_5$ . The substantial discrepancies between experimental and theoretical values

may be attributed to an overestimation of these resonance effects in our theoretical calculations. It is noteworthy that our experimentally observed peaks exhibit good agreement with the scaled MP2/cc-pVTZ frequencies (2927 and 2889 cm<sup>-1</sup>) reported by Lindenmaier et al. [11]. using GAUSSIAN09. However, their assignment of  $\nu_5$  and  $\nu_6$  modes differs from ours, likely due to the fact that they observed fewer peaks in their study. Specifically, they failed to detect the absorption peak around 2943 cm<sup>-1</sup> and, consequently, assigned the peak at 2917 cm<sup>-1</sup> to  $\nu_4$ , whereas we, along with Sharma et al., assign it to  $\nu_5$ . Additionally, they did not observe the peak near 2898 cm<sup>-1</sup> and, instead, assigned the peak at 2862 cm<sup>-1</sup> to  $\nu_6$ .

Lindenmaier et al. attributed the peaks at 2885 and 2862 cm<sup>-1</sup> to  $\nu_5$  and  $\nu_6$ , respectively. In contrast, our analysis assigns the peak at 2885 cm<sup>-1</sup> in the IR spectra of m/z=74 to the overlap of two overtone modes: the methylene scissor  $2\nu_8$  (2928.4 cm<sup>-1</sup>, 9.05 km mol<sup>-1</sup>) and the methyl asymmetric scissor  $2\nu_9$  (2895 cm<sup>-1</sup>, 12.0 km mol<sup>-1</sup>). The excitation in  $2\nu_9$  is less efficient in dissociating the C5-C7 bond, which explains the lower intensity of this peak in the IR spectra of m/z=43 compared to m/z=74. In the IR spectra of m/z=43, the peak near 2885 cm<sup>-1</sup> primarily contributed by  $2\nu_8$ , resulting in a narrower peak profile compared to the IR spectra of m/z=74. Furthermore, the peak at 2866 cm<sup>-1</sup> can be reasonably assigned to the combination modes of methylene CH scissor and methyl symmetric scissor, specifically  $\nu_8+\nu_{10}$  (2890 cm<sup>-1</sup>, 4.75 km mol<sup>-1</sup>).

We have successfully assigned all calculated transitions in the  $2700-3200~{\rm cm}^{-1}$  region, with intensities exceeding 1 km mol<sup>-1</sup>, to the observed peaks, through a thorough examination of both peak position and intensity. However, two predicted transitions,  $2968.6~{\rm cm}^{-1}$  (1.89 km mol<sup>-1</sup>) and  $2950.1~{\rm cm}^{-1}$  (2.27 km mol<sup>-1</sup>), were not detected in the measured IR spectra, likely due to their relatively weak intensities and the presence of nearby strong transitions.

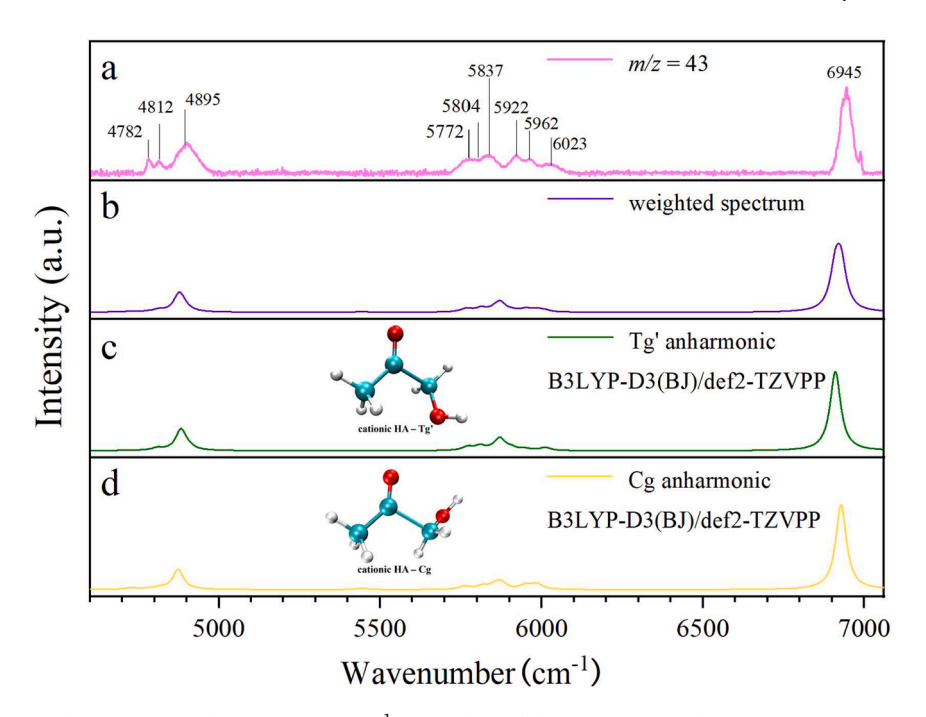


**Fig. 8.** (a) Observed IR spectrum of cationic HA in the 4600 to 7000 cm $^{-1}$  region obtained by monitoring HA fragment cation (m/z = 43). (b) Simulated anharmonic IR spectrum of cationic HA, weighted by 30 % Cg conformer and 70 % Tg' conformer. (c) and (d) the simulated anharmonic IR spectra of the two cationic conformers, Tg' and Cg, respectively, calculated using the VPT2 method at the B3LYP-D3(BJ)/def2-TZVPP level of theory. The stick spectra (Table S6 in the Supporting Information) were convoluted with a Lorentzian profile (FWHM = 40 cm $^{-1}$ ) to generate the final spectra.

For IR laser frequencies exceeding  $3600~\rm cm^{-1}$ , no discernible peaks were observed in the parent ion signal (m/z=74). The lack of change in the parent ion signal upon IR radiation indicates that the photoionization efficiency (PIE) curve of HA exhibits only a slight increase in the energy range of  $10.48-10.79~\rm eV$ , which corresponds to the total energy of a  $125.2~\rm nm$  photon with IR radiation spanning  $4700~\rm to~7200~\rm cm^{-1}$ . As a result, no signal enhancement is observed in this energy range, unlike the case where IR radiation energy falls within the range of  $2700-3600~\rm cm^{-1}$ . The increase in the ionization cross-section of HA due to resonant absorption of IR radiation is counterbalanced by the increase in the dissociative ionization pathway. Therefore, only the IR spectra of HA, obtained by monitoring the signal intensity variation of the fragment ion  $CH_3CO^+(m/z=43)$  in the  $4600-7000~\rm cm^{-1}$  region, are presented, as depicted in Fig. 6a.

In the 4000–7000 cm<sup>-1</sup> region, some vibrational fundamental modes that are unlikely to directly contribute to the dissociation of the C5-C7 bond are observed in the form of combination or overtone modes. This observation is attributed to the reduced mode selectivity in this region, resulting from the increased density of vibrational states that facilitate intramolecular vibrational energy redistribution (IVR). For instance, the density of states of CH<sub>3</sub>CHOO is approximately 5 states/cm<sup>-1</sup> when excited by IR radiation at about 3000 cm<sup>-1</sup> [23], which is close to the threshold vibrational state density required for IVR [35]. As the energy increases, the density of vibrational states rises to 25 states/cm<sup>-1</sup> at 4000 cm<sup>-1</sup> and reaches about 335 states/cm<sup>-1</sup> at 6000 cm<sup>-1</sup> [36].

The spectral region between 4500 and 5500 cm $^{-1}$  exhibits excellent agreement between the observed peak positions and intensities and those calculated, as illustrated in Fig. 6b. However, the peak at 5157 cm $^{-1}$  is an exception, attributed to the combination mode  $\nu_1+\nu_7$ , which was calculated to be located at 5244.3 cm $^{-1}$ , with an intensity of 0.043 km mol $^{-1}$ . The assignment of the observed peaks in this region is summarized in Table 2.

Between 5500 and 7000 cm<sup>-1</sup>, seven distinct spectral features are observed, centered at approximately 5618, 5652, 5768, 5804, 5870, 5934, and 6839 cm<sup>-1</sup>. These features can be attributed to the

combination and overtone vibrational modes of CH and OH stretches, as detailed in Table 2.

## 3.4. IR spectra of cationic HA

The IR spectra of HA cation in the region of  $2700-4200~\rm cm^{-1}$  were obtained by observing the signal variation of the HA cation (Fig. 7a) and its fragment ion m/z=43 (Fig. 7b). The contours of both spectra exhibit a high degree of similarity. However, the IR laser-induced dissociation of the HA cation is evident in Fig. 7a, resulting in the depletion of the HA signal and the concomitant increase of the fragment ion signal at m/z=43. Notably, the IR spectra obtained from observing HA cations exhibit a poor signal-to-noise ratio for absorptions above 3700 cm<sup>-1</sup>, due to the small change in the HA cation signal caused by weak absorption, which is overwhelmed by the large background signal arising from the ionization of HA by the 118 nm laser. Therefore, IR spectra for absorptions above 3700 cm<sup>-1</sup>, obtained from observing HA cations, are not presented.

Although the neutral HA-Cc conformer is dominant in the neutral HA, our calculated IR spectra of the Tg' conformer (Fig. 7d) show better agreement with our experimental observations than those of the Cg conformer (Fig. 7e). To simulate the experimental spectra, we convoluted the stick spectra with Lorentzian profiles (FWHM 40 cm<sup>-1</sup>) to generate the contours. The neutral HA, generated via supersonic expansion, is mainly in the ground vibrational state, with a rotational temperature of approximately 10-20 K. After ionization, the internal energy of the HA cation is primarily derived from the excess energy of 118 nm, which is equivalent to approximately 16.6 kcal mol<sup>-1</sup>. Our calculations reveal that the barrier between the Tg' and Cg conformers is  $2.69\,kcal\,mol^{\text{-}1}$  (Figure S9), suggesting that the internal energy of the HA cation is sufficient to overcome this barrier and redistribute between the two conformers. The insignificant collisional relaxation between HA cations in the molecular beam, combined with the short 100 ns time delay between the VUV and IR laser pulses, justifies the assumption that the conformers are not in thermal equilibrium, and hence, do not follow a Boltzmann distribution. Notably, our simulated spectra (Fig. 7c),

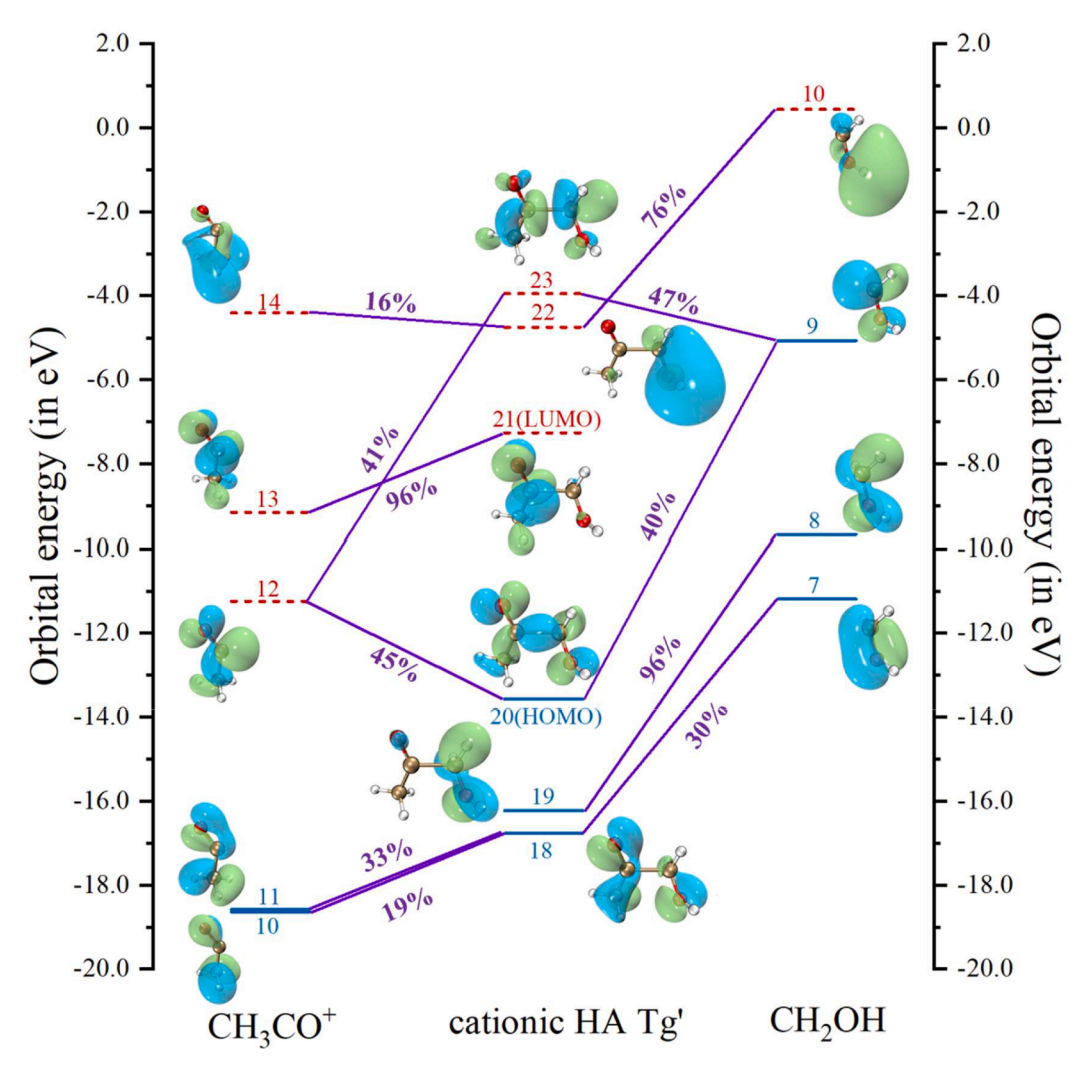


Fig. 9. Orbital interaction analysis diagram for the cationic HA Tg'. Occupied orbitals are shown as blue lines, while unoccupied orbitals are represented by red dashed lines. The major contributions from the fragment molecular orbitals to the HA molecular orbitals (MOs) are indicated by purple lines and text. The MOs are visualized as isosurface graphs with an isovalue of 0.05 au The composition of the MOs was evaluated using the Mulliken population analysis method [37].

weighted by the populations of 30 % Cg and 70 % Tg' conformers, successfully replicate the key spectral patterns and peaks observed in Fig. 7a and 7b.

In the spectral region between 2800 and 3700 cm<sup>-1</sup>, the IR spectra display a distinctive profile characterized by three prominent peaks at 2915, 2984, and 3554 cm<sup>-1</sup>, accompanied by three shoulder features at approximately 2822, 3046, and 3597 cm<sup>-1</sup>. Based on peak positions and intensities, the peaks at 2822, 2915, and 3554 cm<sup>-1</sup> are assigned to fundamental vibration modes, specifically the methylene symmetric CH stretching, methyl out-of-plane symmetric CH stretching, and OH stretching modes, respectively. The remaining three peaks are attributed to absorption from combination or overtone modes. Detailed assignments are provided in Table 3.

The infrared spectrum exhibits a cluster of well-resolved peaks in the  $3800 - 4150 \text{ cm}^{-1}$  region, which can be attributed to  $\nu_{OH}$  vibrational modes. Specifically, peaks are observed at 3883, 3923, 3963, 3998, 4028, 4064, and  $4123 \text{ cm}^{-1}$ . These spectral features are assigned to combination bands (Table S9), as supported by good agreement with theoretical calculations.

The IR spectra of the HA cation in the 4600 to 7000 cm<sup>-1</sup> spectral region are presented in Fig. 8a, accompanied by the calculated IR spectra for the Tg' and Cg conformers (Fig. 8c and 8d) and the weighted IR spectrum (Fig. 8b). The region between 4750 and 5000 cm<sup>-1</sup> exhibits three distinct peaks at 4782, 4812, and 4895 cm<sup>-1</sup>, which are attributed

to combination transitions (Table S9). Specifically, the peak at 4782 cm<sup>-1</sup> is assigned to the combination of the OH stretching and C—O stretching modes,  $v_1 + v_{16}$ , of the Tg' conformer, although the calculated intensity was relatively low at 0.0601 km mol<sup>-1</sup>. This peak appears more intense due to the significant contribution of the C—O stretch (C7-O10) to the C5-C7 bond cleavage. Moreover, the combination of these two modes may induce torsional motion of the CH<sub>2</sub>OH rotor, potentially accelerating the intramolecular vibrational redistribution (IVR) process.

The spectral region between 5700 and 6100 cm<sup>-1</sup> is characterized by CH stretch overtones. However, the high density of fundamental CH stretch modes ( $v_2$  to  $v_6$ ) within this narrow 400 cm<sup>-1</sup> (5700–6100 cm<sup>-1</sup> region) range poses a significant challenge in resolving individual peaks. As a result, the broad feature spanning 5772–5804 cm<sup>-1</sup> is attributed to the cumulative contribution of three transitions: (2 $\nu_6$ ,  $\nu_3 + \nu_4$ , and 2 $\nu_4$ ) from both conformers. Similarly, the peak at 5837 cm<sup>-1</sup> is assigned to the overlapping transitions of  $v_5 + v_6$  and  $2v_3$  from both the Tg' and Cg conformers, which exhibit the strongest intensity in the simulated spectra. The features at 5922 and 5962 cm<sup>-1</sup> are characterized as a combination of  $v_2 + v_3$  (5945 cm<sup>-1</sup>),  $2v_2$  (5954 cm<sup>-1</sup>), and  $2v_5$  (5985 cm<sup>-1</sup> 1) of the Tg' conformer, considering their close resemblance to the experimental contour. Finally, the shoulder peak at 6023 cm<sup>-1</sup> is assigned to the overtone of the methylene asymmetric CH stretch,  $2v_5$ , of the Cg conformer (6010 cm<sup>-1</sup>). The peak at 6945 cm<sup>-1</sup> was attributed to the overtone of OH stretching mode,  $2v_1$ .

Based on the good agreement between the experimental and weighted simulated spectra, we propose that both the Tg' and Cg conformers contribute to the experimental spectra. This observation suggests that ionization triggers rapid energy redistribution in the neutral HA-Cc. Subsequently, approximately 70 % of the CH<sub>2</sub>OH moiety in the HA cation undergoes distortion, attributed to the repulsive force between the positively charged carbonyl oxygen and hydroxyl hydrogen atoms, resulting in the formation of the Tg' conformer. The remaining fraction of the CH<sub>2</sub>OH group in the cationic HA undergoes a conformational change to the Cg conformer, facilitated by the OH wagging motion.

# 3.5. Orbital interaction analysis

The molecular orbitals (MOs) of the cationic HA can be understood as a result of the orbital mixing between the MOs of the  $\mathrm{CH_3CO^+}$  and  $\mathrm{CH_2OH}$  fragments. As an open-shell molecule, the cationic HA has 20 alpha electrons and 19 beta electrons. For the purpose of this analysis, we treat the cationic HA as a complex comprising  $\mathrm{CH_3CO^+}$  and  $\mathrm{CH_2OH}$  fragments. By performing a comprehensive orbital interaction analysis, we gain valuable insights into the cleavage mechanism of the C5-C7 bond.

The closed-shell  $CH_3CO^+$  fragment, with 11 pairs of alpha and beta electrons, exhibits an orbital (numbered 12) that undergoes a bonding-like interaction with orbital 9 of the  $CH_2OH$  fragment, analogous to the bonding process observed in the highest occupied molecular orbital (HOMO), denoted as orbital 20, of the cationic HA, whose energy level is below that of orbital 12 of  $CH_3CO^+$ . In contrast, orbital 23 of orbital 9 in  $CH_2OH$  (Fig. 9).

Upon interaction between the two fragments, the HOMO-1 and the lowest unoccupied molecular orbital (LUMO) of the cationic HA bear a striking resemblance to orbital 13 in  ${\rm CH_3CO^+}$  and orbital 8 in  ${\rm CH_2OH}$ , respectively. These orbitals can be regarded as non-bonding in nature. This orbital diagram provides a rationale for the observed decrease in the Mayer bond order of the C5-C7 bond from 0.96 to 0.56. The Mayer bond order, which is a measure of the electron density between two atoms, indicates that the C—C sigma bond in the HOMO of the cationic HA molecule is occupied by a single electron.

# 4. Conclusion

In this study, we have presented a comprehensive analysis of the vibrational spectra of both neutral and cationic HA molecules in the range of 2700 to 7200 cm<sup>-1</sup>. By employing the NRIFD-IR spectroscopy technique, we successfully obtained the IR spectra of both neutral and cationic HA species and identified their spectral carriers by comparing the observed spectra with computed spectra and structural data. Our findings reveal that neutral HA exists in four distinct equilibrium conformers, with the Cc conformer being the most stable. In contrast, cationic HA exhibits two conformers, Tg' and Cg, which differ significantly from the neutral form in terms of dihedral angles and bond lengths. NBO analysis indicates that the lone pair orbitals of oxygen atoms in cationic HA interact with the antibonding orbital of the C5-C7 bond, leading to a preference for dissociation at this bond. Our findings offer valuable insights into the structural and spectroscopic properties of HA and its cation, as well as shed light on the underlying mechanisms of near-threshold dissociative ionization processes.

# CRediT authorship contribution statement

Ende Huang: Writing – original draft, Validation, Methodology, Formal analysis, Data curation. Siyue Liu: Methodology, Investigation, Data curation. Xiaohu Zhou: Methodology, Data curation. Licheng Zhong: Methodology, Data curation. Shuze Ma: Investigation. Ransheng Wang: Data curation. Hongwei Li: Visualization. Jinrong Yang: Visualization, Methodology. Xiao He: Visualization. Wenrui Dong:

Writing – review & editing, Visualization, Supervision, Project administration, Investigation, Funding acquisition, Formal analysis, Conceptualization. **Xueming Yang:** Visualization.

#### Declaration of competing interest

The authors declare that they have no known competing financial interests or personal relationships that could have appeared to influence the work reported in this paper.

# Data availability

Data will be made available on request.

#### Acknowledgments

The authors gratefully acknowledge the Dalian Coherent Light Source (DCLS) for support and assistance. This work was funded by the National Natural Science Foundation of China (NSFC No. 22288201), the Chinese Academy of Sciences (GJJSTD20220001), and the Innovation Program for Quantum Science and Technology (No. 2021ZD0303305).

## Supplementary materials

Supplementary material associated with this article can be found, in the online version, at doi:10.1016/j.molstruc.2024.139871.

#### References

- A.J. Apponi, J.J. Hoy, D.T. Halfen, L.M. Ziurys, Hydroxyacetone (CH<sub>3</sub>COCH<sub>2</sub>OH): a combined microwave and millimeter-wave laboratory study and associated astronomical search, Astrophys. J. 652 (2) (2006) 1787–1795.
- [2] V. Mohaček-Grošev, Vibrational analysis of hydroxyacetone, Spectrochim. Acta Part A 61 (3) (2005) 477–484.
- [3] Y. Zhou, D.H. Quan, X. Zhang, S.-L. Qin, Detection of hydroxyacetone in protostar IRAS 16293-2422 B, Res. Astron. Astrophys. 20 (8) (2020).
- [4] T.W.G. Solomons, Organic Chemistry, Wiley, New York, 1984.
- [5] D. Grosjean, E.L. Williams, E. Grosjean, Atmospheric chemistry of isoprene and of its carbonyl products, Environ. Sci. Technol. 27 (5) (1993) 830–840.
- [6] J.J. Orlando, G.S. Tyndall, J.M. Fracheboud, E.G. Estupiñan, S. Haberkorn, A. Zimmer, The rate and mechanism of the gas-phase oxidation of hydroxyacetone, Atmos. Environ. 33 (1999) 1621—1629.
- [7] C.A. Taatjes, F. Liu, B. Rotavera, M. Kumar, R. Caravan, D.L. Osborn, W. H. Thompson, M.I. Lester, Hydroxyacetone production from C(3) criegee intermediates, J. Phys. Chem. A 121 (1) (2017) 16–23.
- [8] R. Lindenmaier, S.D. Williams, R.L. Sams, T.J. Johnson, Quantitative infrared absorption spectra and vibrational assignments of crotonaldehyde and methyl vinyl ketone using gas-phase mid-infrared, far-infrared, and liquid raman spectra: s-cis vs s-trans composition confirmed via temperature studies and ab initio methods, J. Phys. Chem. A 121 (6) (2017) 1195–1212.
- [9] T.J. Dillon, A. Horowitz, D. Holscher, J.N. Crowley, L. Vereecken, J. Peeters, Reaction of HO with hydroxyacetone (HOCH<sub>2</sub>C(O)CH<sub>3</sub>): rate coefficients (233-363 K) and mechanism, Phys. Chem. Chem. Phys. 8 (2) (2006) 236–246.
- [10] A. Sharma, I. Reva, R. Fausto, Matrix-isolation study and Ab initio calculations of the structure and spectra of hydroxyacetone, J. Phys. Chem. A 112 (2008) 5935–5946.
- [11] R. Lindenmaier, N. Tipton, R.L. Sams, C.S. Brauer, T.A. Blake, S.D. Williams, T. J. Johnson, Assignment of the fundamental modes of hydroxyacetone using gas-phase infrared, far-infrared, raman, and ab initio methods: band strengths for atmospheric measurements, J. Phys. Chem. A 120 (30) (2016) 5993–6003.
- [12] B.P. Gordon, F.G. Moore, L.F. Scatena, N.A. Valley, S.N. Wren, G.L. Richmond, Model behavior: characterization of hydroxyacetone at the air-water interface using experimental and computational vibrational sum frequency spectroscopy, J. Phys. Chem. A 122 (15) (2018) 3837–3849.
- [13] X.H. Zhou, E.D. Huang, L.C. Zhong, S. Liu, S. Ma, H. Li, X. Yang, W. Dong, Vibrational spectroscopy of neutral and cationic 2-Methoxyethanol, J. Mol. Struct. 1294 (2023).
- [14] W.W. Fei, Ming. Wang, Jun. Chen, Z.H. Li, Y.P. Yu, X. Lin, F.Y. Liu, X.B. Shan, L. S. Sheng, Vacuum ultraviolet ionization and dissociation of hydeoacetone, Chinese Journal of quantum electronics 35 (2018) 513–522.
- [15] R. Arakawa, Mass spectral study of ionized-Hydroxyacetone dissocciation, Chem. Society of Japan 64 (1990) 1022–1024.
- [16] T. Lu, Molclus Program 2022, Beijing Kein Research Center for Natural Science, China, 2022. http://www.keinsci.com/research/molclus.html.

- [17] S. Grimme, J. Antony, S. Ehrlich, H. Krieg, A consistent and accurate ab initio parametrization of density functional dispersion correction (DFT-D) for the 94 elements H-Pu, J. Chem. Phys. 132 (15) (2010) 154104.
- [18] M. Sierka, A. Hogekamp, R. Ahlrichs, Fast evaluation of the Coulomb potential for electron densities using multipole accelerated resolution of identity approximation, J. Chem. Phys. 118 (20) (2003) 9136–9148.
- [19] S. Grimme, S. Ehrlich, L. Goerigk, Effect of the damping function in dispersion corrected density functional theory, J. Comput. Chem. 32 (7) (2011) 1456–1465.
- [20] M.J. Frisch, G. W. Trucks, H.B. Schlegel, G.E. Scuseria, M.A. Robb, J.R. Cheeseman, G. Scalmani, V. Barone, G.A. Petersson, X.L. H, M. Nakatsuji, A.V. Caricato, J. Marenich, B.G. Bloino, R. Janesko, B. Gomperts, H.P. Mennucci, J.V. Hratchian, A. F. Ortiz, J.L. Izmaylov, D. Sonnenberg, F. Williams-Young, Ding, F. Lipparini, F. Egidi, J. Goings, B. Peng, A. Petrone, T. Henderson, D. Ranasinghe, V.G. Zakrzewski, J. Gao, N. Rega, G. Zheng, W. Liang, M. Hada, M. Ehara, K. Toyota, R. Fukuda, J. Hasegawa, M. Ishida, T. Nakajima, Y. Honda, O. Kitao, H. Nakai, T. Vreven, K. Throssell, J.A. Montgomery Jr., J.E. Peralta, F. Ogliaro, M.J. Bearpark, J.J. Heyd, E.N. Brothers, K.N. Kudin, V.N. Staroverov, T.A. Keith, R. Kobayashi, J. Normand, K. Raghavachari, A.P. Rendell, J.C. Burant, S.S. Iyengar, J. Tomasi, M. Cossi, J.M. Millam, M. Klene, C. Adamo, R. Cammi, J.W. Ochterski, R.L. Martin, K. Morokuma, O. Farkas, J.B. Foresman, D.J. Fox, Gaussian 16, Revision A.03, Gaussian Inc., Wallingford, CT, 2016.
- [21] F. Neese, The ORCA program system, WIREs Computat. Molecular Sci. 2 (1) (2011) 73–78
- [22] A.S. Hansen, T. Bhagde, K.B. Moore III, et and, Watching a hydroperoxyalkyl radical (•QOOH) dissociate, Science 373 (6555) (2021) 679–682.
- [23] V.P. Barber, S. Pandit, V.J. Esposito, A.B. McCoy, M.I. Lester, CH Stretch Activation of CH<sub>3</sub>CHOO: deep Tunneling to Hydroxyl Radical Products, J. Phys. Chem. A 123 (13) (2019) 2559–2569.
- [24] T. Lu, F. Chen, Multiwfn: a multifunctional wavefunction analyzer, J. Comput. Chem. 33 (5) (2012) 580–592.
- [25] W. Humphrey, A. Dalke, K. Schulten, VMD: visual Molecular Dynamics, J Mol Graph 14 (1) (1996) 33–38.

- [26] A.F. Jalbout, F.F. Contreras-Torres, L. Adamowicz, The hydroxyacetone (CH<sub>3</sub>COCH<sub>2</sub>(OH)) torsional potential and isomerization: a theoretical study, Int. J. Quantum Chem. 108 (2) (2007) 279–288.
- [27] K. Kimura, S. Katsumata, Y. Achiba, T. Yamazaki, S. Iwata. Handbook of HeI Photoelectron Spectra of Fundamental Organic molecules: Ionization energies, Ab Initio assignments, and Valence Electronic Structure For 200 Molecules, Japan Scientific Societies Press, Tokyo, 1981.
- [28] F.P. Lossing, Heats of formation of some isomeric  $[C_nH_{2n+1}O]^+$  ions. Substitutional effects on ion stability, J. Am. Chem. Soc. 99 (23) (1977) 7526–7530.
- [29] P.C. Burgers, J.L. Holmes, J.K. Terlouw, B. van Baar, Three new isomers of [C<sub>2</sub>H<sub>6</sub>O] <sup>†</sup>: the radical cations [CH<sub>3</sub>O(H)CH<sub>2</sub>]<sup>†</sup>, [CH<sub>3</sub>CHOH<sub>2</sub>]<sup>†</sup> and a low-energy isomer of unassigned structure, Org. Mass Spectrom. 20 (3) (2005) 202–206.
- [30] J.L. Holmes, F.P. Lossing, Heats of formation of organic radicals from appearance energies, Int. J. Mass Spectrom. Ion Process. 58 (1984) 113–120.
- [31] B. Chan, L. Radom, Frequency scale factors for some double-hybrid density functional theory procedures: accurate thermochemical components for high-level composite protocols, J. Chem. Theory Comput. 12 (8) (2016) 3774–3780.
- [32] P. A, R.L. Scott, Harmonic vibrational frequencies: an evaluation of hartree-fock, møller-plesset, quadratic configuration interaction, density functional theory, and semiempirical scale factors, J. Phys. Chem. 100 (41) (1996) 16502–16513.
- [33] C. Ceźard, C.A. Rice, M.A. Suhm, OH-Stretching Red shifts in bulky hydrogenbonded alcohols: jet spectroscopy and modeling, J. Phys. Chem. A 110 (2006) 9839–9848.
- [34] Y.J. Hu, H.B. Fu, E.R. Bernstein, Infrared plus vacuum ultraviolet spectroscopy of neutral and ionic ethanol monomers and clusters, J. Chem. Phys. 125 (15) (2006) 154305
- [35] K.K. Lehmann, G. Scoles, B.H. Pate, Intramolecular dynamics from eigenstateresolved infrared spectra, Annu. Rev. Phys. Chem. 45 (1) (1994) 241–274.
- [36] Y. Fang, F. Liu, V.P. Barber, S.J. Klippenstein, A.B. McCoy, M.I. Lester, Deep tunneling in the unimolecular decay of CH<sub>3</sub>CHOO Criegee intermediates to OH radical products, J. Chem. Phys. 145 (23) (2016) 234308.
- [37] T. Lu, F.W. CHEN, Calculation of molecular orbital composition, Acta Chim. Sinica 69 (20) (2011) 2393–2406.